

# Electrohydrodynamic Bubbling: An Alternative Route to Fabricate Porous Structures of Silk Fibroin Based Materials

Zeynep Ekemen,<sup>†</sup> Zeeshan Ahmad,<sup>‡</sup> Eleanor Stride,<sup>†,§</sup> David Kaplan,<sup>\*,||</sup> and Mohan Edirisinghe<sup>\*,†</sup>

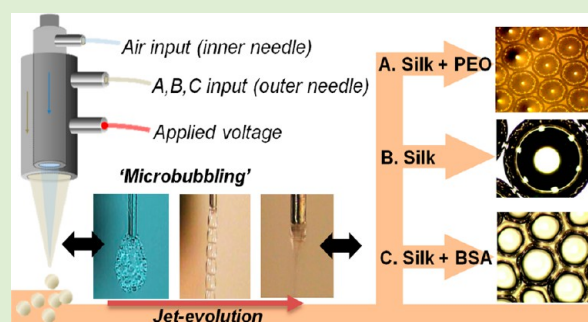
<sup>†</sup>Department of Mechanical Engineering, University College London, Torrington Place, London WC1E 7JE, United Kingdom

<sup>‡</sup>School of Pharmacy and Biomedical Sciences, University of Portsmouth, St. Michael's Building, White Swan Road, Portsmouth, PO1 2DT, United Kingdom

<sup>§</sup>Institute of Biomedical Engineering, Old Road Campus Research Building, University of Oxford, Oxford OX3 7DQ, United Kingdom

<sup>||</sup>Department of Biomedical Engineering, Tufts University, Boston, Massachusetts 02155, United States

**ABSTRACT:** Conventional fabrication techniques and structures employed in the design of silk fibroin (SF) based porous materials provide only limited control over pore size and require several processing stages. In this study, it is shown that, by utilizing electrohydrodynamic bubbling, not only can new hollow spherical structures of SF be formed in a single step by means of bubbles, but the resulting bubbles can serve as pore generators when dehydrated. The bubble characteristics can be controlled through simple adjustments to the processing parameters. Bubbles with diameters in the range of 240–1000  $\mu\text{m}$  were fabricated in controlled fashion. FT-IR characterization confirmed that the rate of air infused during processing enhanced  $\beta$ -sheet packing in SF at higher flow rates. Dynamic mechanical analysis also demonstrated a correlation between air flow rate and film tensile strength. Results indicate that electrohydrodynamically generated SF and their composite bubbles can be employed as new tools to generate porous structures in a controlled manner with a range of potential applications in biocoatings and tissue engineering scaffolds.



## INTRODUCTION

Fabrication of silk fibroin (SF) structures derived from *Bombyx mori* is utilized in various areas of biomedical applications: from tissue engineering scaffolds<sup>1</sup> to microfluidic devices.<sup>2</sup> Its popularity is largely due to the materials excellent mechanical properties<sup>3</sup> and controllable biodegradation.<sup>4</sup> In addition, the degree of  $\beta$ -sheet nanocrystals within the SF structure can be tightly controlled at various stages of the fabrication process and, in fact, even at the extraction stage. Postfabrication treatment with chemicals also provides further opportunities in optimizing the  $\beta$ -sheet crystal structure. Though structures from pure SF have shown a wide range of applications, many silk composites have been prepared using, that is, hydroxyapatite,<sup>5</sup> chitosan,<sup>6</sup> gelatin,<sup>7</sup> and polyurethane,<sup>8</sup> as potential materials for soft and hard tissue engineering. Incorporation of such materials offers numerous advantages including enhanced control over the release of biological molecules and the possibility to combine both precise control of temporal and spatial biological signals and physical/mechanical cues in a single construct.<sup>9</sup>

Up to now, gels, films, microspheres, fibers, sponges, and tube structures comprising SF have been successfully generated using various techniques.<sup>10</sup> However, much focus has been directed toward the production of porous structures for tissue engineering purposes. One process of obtaining this is by using fibers to generate mats that can deliver a range of pore sizes

from a variety of materials, and this has currently been shown using the electrospinning process.<sup>11–14</sup> The electrohydrodynamic (EHD) process, which also underpins the electrospinning phenomenon, is the formation of a jet when flowing media are subjected to an applied electric field. At the jet break-up point, micrometer and nanometer size structures can be formed and their shape is dependent on material properties and system parameters.<sup>15–17</sup> The underlying method is adaptable and robust; alteration to the set up facilitates EHD printing,<sup>18</sup> micro/nano encapsulation,<sup>19</sup> and also the microbubbling processes.<sup>20</sup> Microbubbling using EHD is achieved when air flow is utilized as the inner medium and solution flow is directed through the outer needle, whereby the rate of infusion is controlled. Liquid and gas phase coflow through the concentrically aligned needles are independent of each other and only come into contact at the device orifice, where ultimately the liquid-phase material encapsulates the air, resulting in bubble structures. The shell thickness, bubble size, distribution, and output rates can be controlled and optimized by the system parameters, that is, flow rate and applied voltage. Microbubble fabrication has drawn considerable interest in the fields of ultrasound contrast agents<sup>21</sup> and

Received: January 14, 2013

Revised: March 22, 2013

Published: March 28, 2013

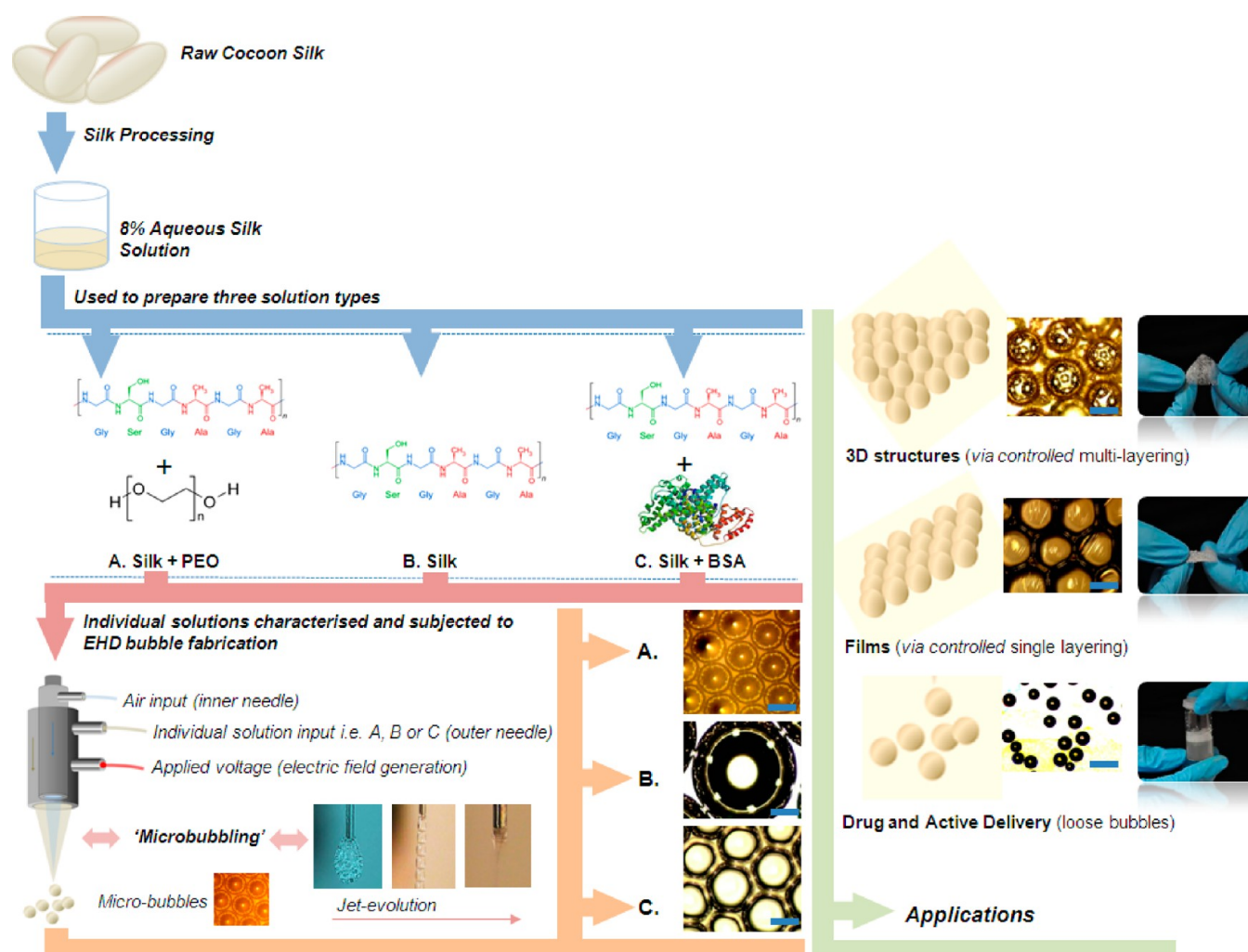


**Figure 1.** Illustration of the silk preparation process, fabrication of bubbles using electrohydrodynamic microbubbling, and resulting structures with envisioned applications. Scale bars on optical images are 200  $\mu\text{m}$ .

drug delivery;<sup>22</sup> however, their range of potential biomedical applications is much broader and now encompasses templates for porous structures.<sup>23,24</sup>

Recently, bovine serum albumin (BSA) bubbles prepared via EHD-microbubbling were used as templates to fabricate 3D, 2D, and standalone bubble structures with potential biomedical applications.<sup>25</sup> SF has been fabricated with various other processing methods other than spinning in the preparation of porous structures, such as salt leaching,<sup>26</sup> freeze-drying, and gas foaming.<sup>27</sup> However, a key challenge that remains during these processes is the homogeneity and interconnectivity between pores in such structures.

In this work, we introduce EHD-microbubbling as an alternative route for the preparation of SF structures. Closely packed deposition of bubbles transforms into a stable porous structure when air-dried, with pores corresponding to the air voids and the connected strut frames to the shells of the initial bubble structures. Deposition of a single layer bubble, when solidified, results in a porous film, and a layer by layer deposition of bubbles forms a scaffold-like network as they build up, which can be used as a template for porous 3D and 2D structures.

For the first time, we demonstrate the generation of microbubbles and bubbles coatings with various silk solutions

(pure SF, SF/polyethylene oxide (PEO), and SF/BSA) using the microbubbling process without any chemical modifications. Other than the variance in solution properties and rheology, the size and distribution can be controlled through parametric optimization of the microbubbling process to reach a near-monodisperse pore size. SF porous films were also tested for their tensile strength and for the analysis of their secondary structures.

## MATERIALS AND METHODS

**Materials.** *Bombyx mori* silk cocoons were purchased from Set Francis, Devon, U.K. Lithium bromide (LiBr;  $\geq 99\%$ ), sodium carbonate ( $\text{Na}_2\text{CO}_3$  anhydrous,  $\geq 99\%$ ), bovine serum albumin (BSA;  $>96.0\%$  lyophilized powder, essentially fatty acid free and globulin free), phosphate buffered saline (PBS; one tablet in 200 mL of distilled water gives 137 mM NaCl, 2.7 mM KCl, and 10 mM phosphate buffer solution), and polyethylene oxide (PEO,  $M_w \sim 100000$  g/mol) were purchased from Sigma-Aldrich Co. Ltd. Dorset, U.K. The Slide-A-Lyzer 3.5 K dialysis cassettes were purchased from Thermo Fisher Scientific Inc., Rockford, U.S.A.

**Methods. Preparation of Regenerated SF Solution.** SF was extracted according to the process described by Jin et al.<sup>28</sup> *Bombyx mori* silk cocoons were initially degummed to remove the glue-like sericin proteins. This was achieved by boiling the cocoons in water containing 0.02 M  $\text{Na}_2\text{CO}_3$  for 30 min, followed by a thorough rinse with distilled water. The boiling procedure was repeated once with

pure water; the silk was rinsed and dried and 5 g of it was dissolved gently in 25 mL of 9.3 M LiBr solution at 60 °C. To remove the salt, the resultant solution was dialyzed against distilled water using a Slide-A-Lyzer dialysis cassette over 3 days at the ambient temperature (25 °C), and the water was changed each day. Debris was removed from the final silk solution until clear and the concentration was calculated to be ~8 wt % by weighing a dried sample of a known volume.

**Preparation of Microbubbling Solutions.** Three different solutions were utilized for microbubbling; aqueous silk, SF-BSA solution (1:1 volume ratio), and SF-PEO blend (4:1 volume ratio). A 20 wt % BSA solution was prepared using PBS. PEO solution was prepared by dissolving 4 wt % PEO in deionized water. Solutions were stirred gently at the ambient temperature until complete dissolution of the solutes was achieved.

**Solution Characterization.** Various silk solutions were characterized for their surface tension and viscosity, immediately after preparation. Surface tension was measured using a Kruss Tensiometer K9 (Krüss GmbH, Hamburg, Germany). Rheology was carried out at a controlled shear-rate with a cone and plate geometry (2° cone angle, 55 mm cone diameter) using a Gemini 150 HR nano rheometer (Malvern Bohlin Instruments, Malvern, U.K.). All measurements were performed at ambient temperature and repeated three times.

**Structural Characterization.** Bubbles were collected on glass microscope slides. Bubbles and their resulting structures were observed using a Nikon Eclipse ME600 optical microscope. Scanning electron microscopy (Hitachi S-3400N SEM, at an accelerating voltage of 15 kV) and Fourier-transform infrared spectroscopy were utilized to assist in structural characterization. SEM samples were gold coated by a sputtering machine (Edwards Sputter coater S150B) for 2 min to enable conduction in the sample and prevent charging. The samples were then placed on an aluminum stub and placed in the SEM chamber. The diameter of the pores and struts were measured using the image-processing program UTHSCSA Image Tool (Image Tool, version 2, U.S.A.). FT-IR spectra of cast SF and microbubbled SF films were obtained using a Perkin-Elmer System 2000 FT-IR spectrometer (PerkinElmer Life and Analytical Sciences, Inc., Wellesley, MA, U.S.A.). The polydispersity index (PI) was calculated as standard deviation/mean of the bubble size distribution.

**Mechanical Testing.** Dynamic mechanical analysis (DMA, Q800 Series, TA Instruments, New Castle, DE, U.S.A.) was used to perform tensile tests on films. Films with equivalent sizes (40 × 15 mm<sup>2</sup>) were placed in tension between a fixed and moveable clamp. A preload force of 0.005 N was used with a force ramp rate of 3 N/min up to 18 N and results were analyzed using Universal Analysis 2000 software.

**Experimental Setup.** Figure 1 represents an overall illustration of the SF solution preparation, combination of materials used in this study, the coaxial device with the process of microbubbling, and finally a general insight on the structures (single bubble, single layered, and multilayered) fabricated and their applications. Air was infused through the inner nozzle of the stainless steel coaxial device and protein solutions were infused through the outer nozzle using a precision syringe pump (Harvard Apparatus, Edenbridge, U.K.) through silicone tubing. The coaxial device consisted of an inner nozzle of 1.9 mm and an outer nozzle of 2.2 mm. The inner needle exit was placed 2 mm above the exit of the outer needle. As both materials are allowed to flow simultaneously with optimized infusion rates, the air becomes encapsulated with the protein solution at the orifice; forming bubbles. These bubbles were further improved by subjecting the flow to an electric field using a high voltage (kV) coupled to the needles (Glassman Europe Ltd., Bramley, U.K.).

## RESULTS AND DISCUSSION

**Solution Properties.** The physical properties of the solution determines its jetting behavior and modes of flow under an applied electrical field. During EHD processing, formation of a stable jet becomes difficult with high surface tension, therefore solvents or solutions having a surface tension less than ~70 mN m<sup>-1</sup> are desirable. A protein with higher molecular weight will possess a lower surface tension.<sup>29</sup> The

molecular weight of BSA is approximately 66.5 kg/mol and that of SF can vary up to 391 kg/mol. Due to the BSA solution's high surface tension (65 mN m<sup>-1</sup>) it was demonstrated that the microbubbling process of BSA was more controlled when the phosphate buffered saline (PBS) used as the solvent was partially substituted by small additions of ethanol, which in turn reduced the overall surface tension of the aqueous protein solution.<sup>25</sup> The BSA and SF mixture exhibited an acceptable surface tension of ~54 mN m<sup>-1</sup>, which automatically eliminated the need for a secondary solvent to reduce the surface tension. As BSA is a model protein, the aim is to make silk a more biocompatible matrix compared to structures composed of SF alone providing additional binding sites. PEO is a widely used polymer for aiding the electrospinning process by increasing the viscosity of the solution.<sup>30</sup> For these reasons, the addition of 4 wt % PEO at a 4:1 SF/PEO volume ratio was chosen to determine its effects on the processability and also on the bubble structure size and distribution.

**Rheology of SF Solutions.** Figure 2 displays the rheology of pure SF, SF/BSA, and SF/PEO blends.

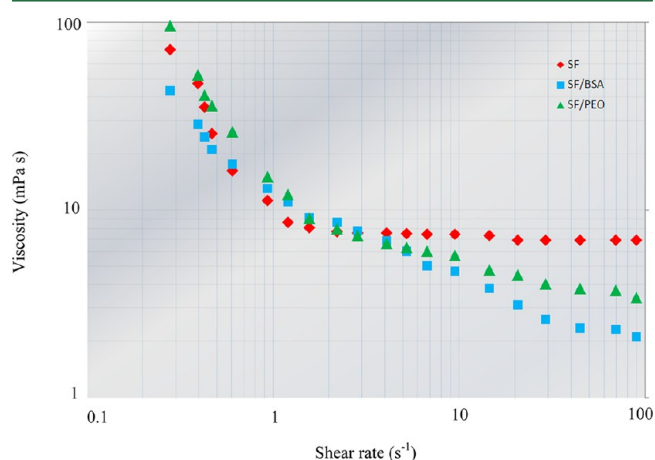


**Figure 2.** Plot of viscosity against shear rate for pure SF, SF/BSA, and SF/PEO blends.

Initially, SF exhibited rapid shear thinning, and at higher shear rates, the non-Newtonian behavior was followed by a near constant viscosity. Thus, the silk macromolecule demonstrates a Newtonian behavior at shear rates >2 s<sup>-1</sup>. The initial significant drop in viscosity and the subsequent Newtonian behavior of SF is governed by the amphiphilic nature of SF in an aqueous environment.<sup>31</sup> SF is a copolymer consisting of light and heavy chains. The heavy chains are composed of 12 repeating oligo-peptide domains and 11 amorphous, more hydrophilic spacers.<sup>32</sup> The onset of shear at lower rates, breaks the hydrogen bonds in SF, leading to the unfolding of chains thus allowing the formation of aggregates. The free fibroin chains, once subjected to high shear, form intermolecular interactions, and the hydrophobic domains self-organize into  $\beta$ -sheet structures mediated by hydrophobic hydration, preventing self-organization and, thus, aggregation,<sup>33,34</sup> observed in the Newtonian behavior, that is, the plateau observed at the end.

Figure 2 indicates the addition of BSA and PEO markedly reduced the viscosity of SF at shear rates >3 s<sup>-1</sup>. As an important constituent of blood; serum albumins exhibit a shear thinning rheological response. The SF/BSA contains a higher concentration of BSA protein (20 wt %) than SF protein (8 wt %), which clearly interferes with the self-assembly; this can be



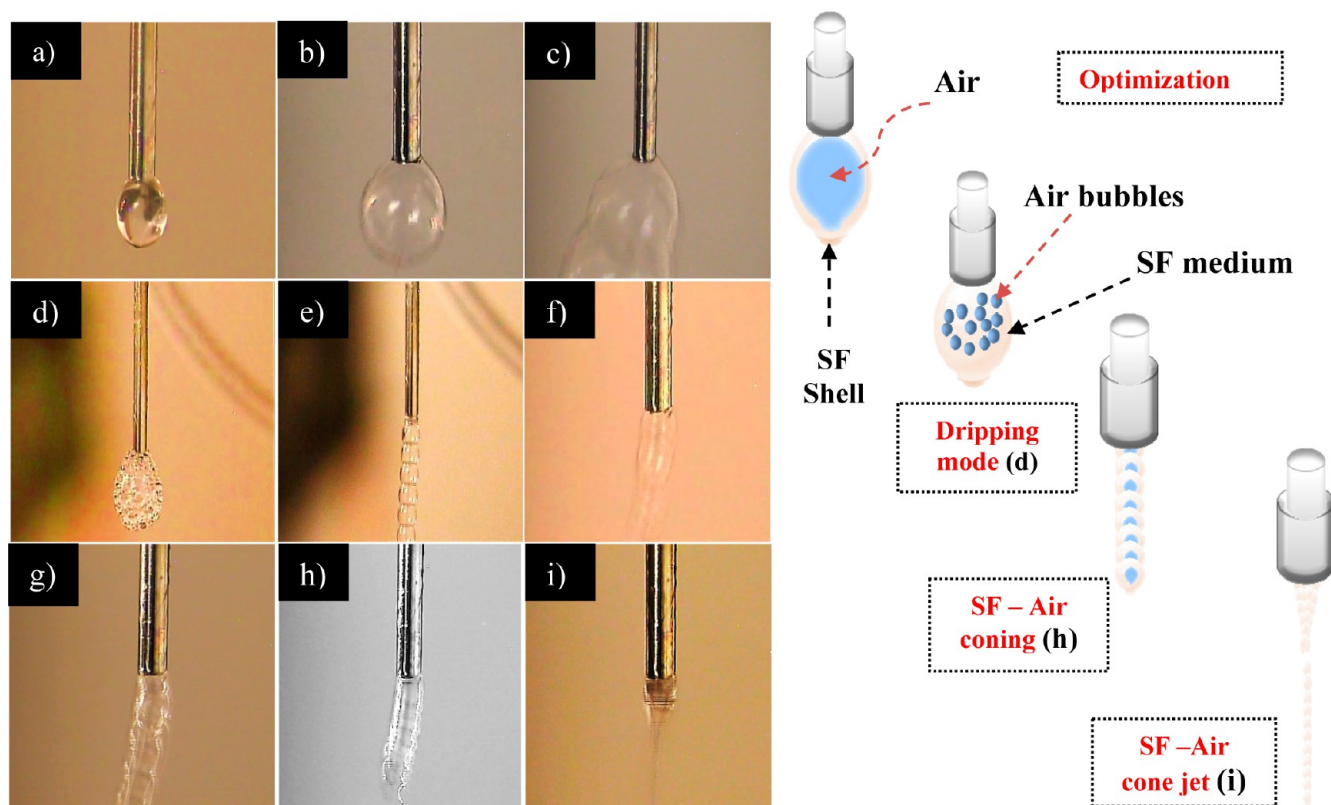


**Figure 3.** Representation of the modes of SF microbubbling, actual and schematic: (a) SF flow with no air; (b) infusion of air, bubble expansion is seen due to the flexibility of SF; (c) subjected to an electric field; (d) the dripping mode; (e) subjected to an electric field (1–10 kV); (f) unstable coning mode; (g) approach of coning mode; (h) coning mode (13 kV); and finally, (i) microbubbling mode (air-cone jet) mode is established (18 kV).

due to the inhibition of the alignment of free SF chains either by the placement of the globular proteins (BSA) around the fibroin chains (SF) or by an overall molecular entanglement between the fibrous chains and the globular proteins. The 4:1 SF/PEO blend also illustrates shear thinning behavior due to PEO elasticity and increased hydrophobic interactions due to PEOs hydrophilic nature. The hydrophilic polymer slows down the alignment of SF chains at the high end of applied shear rate.

**Modes of Microbubbling and the Process.** Modes of microbubbling differ from those of different types of conventional liquid spraying and spinning modes. Pioneering studies conducted by Farook et al.<sup>35,36</sup> demonstrated that the microbubbling process is characterized by three modes, bubble dripping, coning, and microbubbling, caused by the presence of an air flow instead of a liquid flow through the inner needle. Without the use of any air flow the conventional dripping mode (Figure 3a) will occur. Optimization of the processing parameters in this study was necessary to obtain the final microbubbling mode as SF displays various modes before forming a stable jet. Initial explorations demonstrated that aqueous SF has tendencies to spin rather than bubble. Low SF flow rates ( $<60 \mu\text{L min}^{-1}$ ) failed to produce any bubbles, whereas above  $60 \mu\text{L min}^{-1}$  (with air flow rates between 100 and  $200 \mu\text{L min}^{-1}$ ), large bubbles were generated. Low infusion rates of both air and SF solution caused a constant expansion of the SF shell (Figure 3b) until it burst. Applying an electric field at this point (Figure 3c) between 18 and 20 kV resulted in an extremely unstable coning mode whereby the formation of the next (single) bubble was deferred for a long time. Therefore, optimization was required for the dripping mode. Increasing

the SF flow rate resulted in smaller air bubbles inside the SF medium and the bubbles detached from the orifice once the gravitational force overcomes the surface tension force. A new drop with air bubbles starts forming straight after and this is the dripping mode (Figure 3d) at zero voltage.

Normally, when an electric field is applied, the coning mode is expected to appear. However, applying an electric field (1–10 kV) brought about a preferential constant flow of a chain of bubbles or bubble tracks from the orifice of the needle (Figure 3e), whereby each bubble was vertically placed above one another with the same size and geometry. This is a new phenomenon with proteinaceous solutions, which has not been observed with other systems, such as phospholipid<sup>36</sup> or glycerol<sup>20</sup> EHD-microbubbling. This, therefore, can be directly attributed to the physical properties of the protein, and each proteinaceous solution would expect to give a similar “interim-mode” before coning. Figure 3f–i represents the optimization process before the microbubbling mode is established. This was achieved by increasing the voltage. At 13 kV, the SF-air coning mode took place (Figure 3h) and further increments to 18 kV resulted in the SF-air cone-jet (Figure 3i). It should be noted that microbubbling modes in proteinaceous mediums can appear in more than one stage. The optimization values given in this instance was from the lowest flow rates; once the ratio between air and liquid medium is ideal, the microbubbling can be conducted resulting in various size and size distributions. Generation of uniform bubbles is highly desirable, especially when the final assembly needs to have controlled pore size and structure. EHD-microbubbling offers this capability, along with high output rates, in a single step. During the microbubbling of

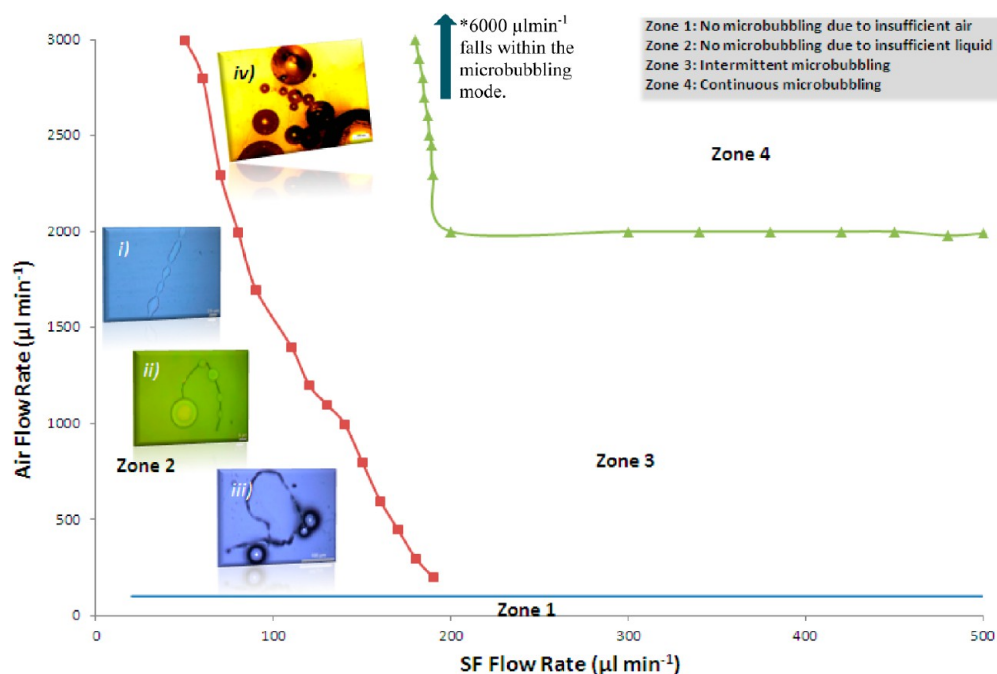


**Figure 4.** Parametric plot between the air flow rate and the flow rate of silk fibroin solution. Images represent the optimization process from fibers to silk bubbles by varying flow rate and applied voltage: (i, ii) aq. SF fibrous structures; (iii) toward optimization resulting in bubbles with fibers; (iv) bubble formation with gelling effects of the SF.

aqueous SF and SF blends, instabilities were encountered, therefore, for all the solutions, parameters were determined with respect to flow rates of the mediums (both air and SF solutions) and applied voltage. Further optimization was necessary within each parametric set to avoid transitions toward unwanted modes and also for a uniform size. Bubbling of SF/BSA and SF/PEO was optimized to achieve the stable air-cone jet mode, as represented in Figure 3i for pure SF. The collection distance was fixed at 100 mm from the orifice of the needle to the collecting point, and a layer of bubbles were collected on glass slides for analysis.

**Microbubbling of Aqueous SF.** The parametric plot constructed between the air flow rate and the flow rate of SF solution is shown in Figure 4. It was not possible to observe the microbubbling mode below the minimum critical air flow rate of  $100 \mu\text{L min}^{-1}$  as the air flow rate was insufficient in the region indicated as Zone 1. Similarly, there was no microbubbling taking place in the region indicated as Zone 2 due to insufficient liquid flow rate (starting at  $60 \mu\text{L min}^{-1}$  with high air flow rates). Initially, and SF flow rate of  $50 \mu\text{L min}^{-1}$  did not suffice for bubble formation even under high air flow rates of up to  $3000 \mu\text{L min}^{-1}$ . As the voltage was applied the air caused turbulent flow which resulted in multiple jet formation, a phenomena commonly associated with conventional EHD processing, resulting in fibrous structures (Figure 4i,ii). Increasing the SF flow rate to a  $100 \mu\text{L min}^{-1}$  (above a threshold of  $1500 \mu\text{L min}^{-1}$  air flow rate) formed few bubbles along with fibers (Figure 4iii).

Bubbling commenced when the flow rate of SF was increased. With the air flow rate ( $6000 \mu\text{L min}^{-1}$ ), bubbling commenced at  $\sim 15$  kV, however, due to the gelling effect of SF under high pressure, the bubbles adhered to the orifice of the needle and the processing halted due to clogging at the device exit (Figure 4iv). Bubbles formed with SF flow rates up to  $100 \mu\text{L min}^{-1}$  were very polydisperse; therefore, lower flow rates (of SF) are automatically eliminated to ease the collection and to

establish modes of the microbubbling system for aqueous SF. SF flow rates of up to  $200 \mu\text{L min}^{-1}$  with various air flow rates and voltage resulted in either no bubble formation (fiber formation) or nonuniform structures. Continuing with a systematic increase of the parameters, SF flow rate of  $200 \mu\text{L min}^{-1}$  generated near monodisperse bubbles ( $\text{PI} \sim 10$ ) with an air flow rate of  $2000 \mu\text{L min}^{-1}$  between 18 and 24 kV. When the air flow rate was kept constant and SF flow was increased by increments of  $100 \mu\text{L min}^{-1}$ , the bubble diameter decreased (Figure 5a–d) and the bubble shell thickness (struts) increased (Figure 5e–h). Increasing the SF flow rate from 200 to  $1000 \mu\text{L min}^{-1}$  reduced the bubble size from  $\sim 1$  mm to  $\sim 600 \mu\text{m}$ . However, increasing the voltage up to 24 kV reduced bubble size with the excess SF contributing toward the bubbles shell thickness. Using SEM (Figure 5i–m), it was also observed that bubbles with coarser shells maintained a circular dimension, whereas those with thinner coatings may have experienced “buckling”, giving rise to other shapes prior to solidification. However, all bubbles remained stable until the samples were dried under ambient conditions. When the flow rate of air was increased up to  $6000 \mu\text{L min}^{-1}$  with a constant SF flow rate of  $200 \mu\text{L min}^{-1}$ , the bubbles increased in size and shell thickness decreased linearly at  $\sim 15$  kV.

**Microbubbling of SF/PEO.** Compared to SF only, considerably fewer instabilities were encountered with microbubbling of SF/PEO, and the transition between the microbubbling modes was established without difficulty (Figure 6). Thus, it was clear that the addition of PEO made the microbubbling process easier.

This could be attributed to a higher viscosity and surface tension ( $58 \text{ mN m}^{-1}$ ) of the blend compared to aqueous SF ( $50 \text{ mN m}^{-1}$ ) and the prevention of any gelling effects SF might have had during the liquid medium flow through the nozzle. PEO is a biocompatible polymer and was chosen as a blending agent because of this and due to it being soluble in water. Here it was selected to ease the processing of aqueous SF



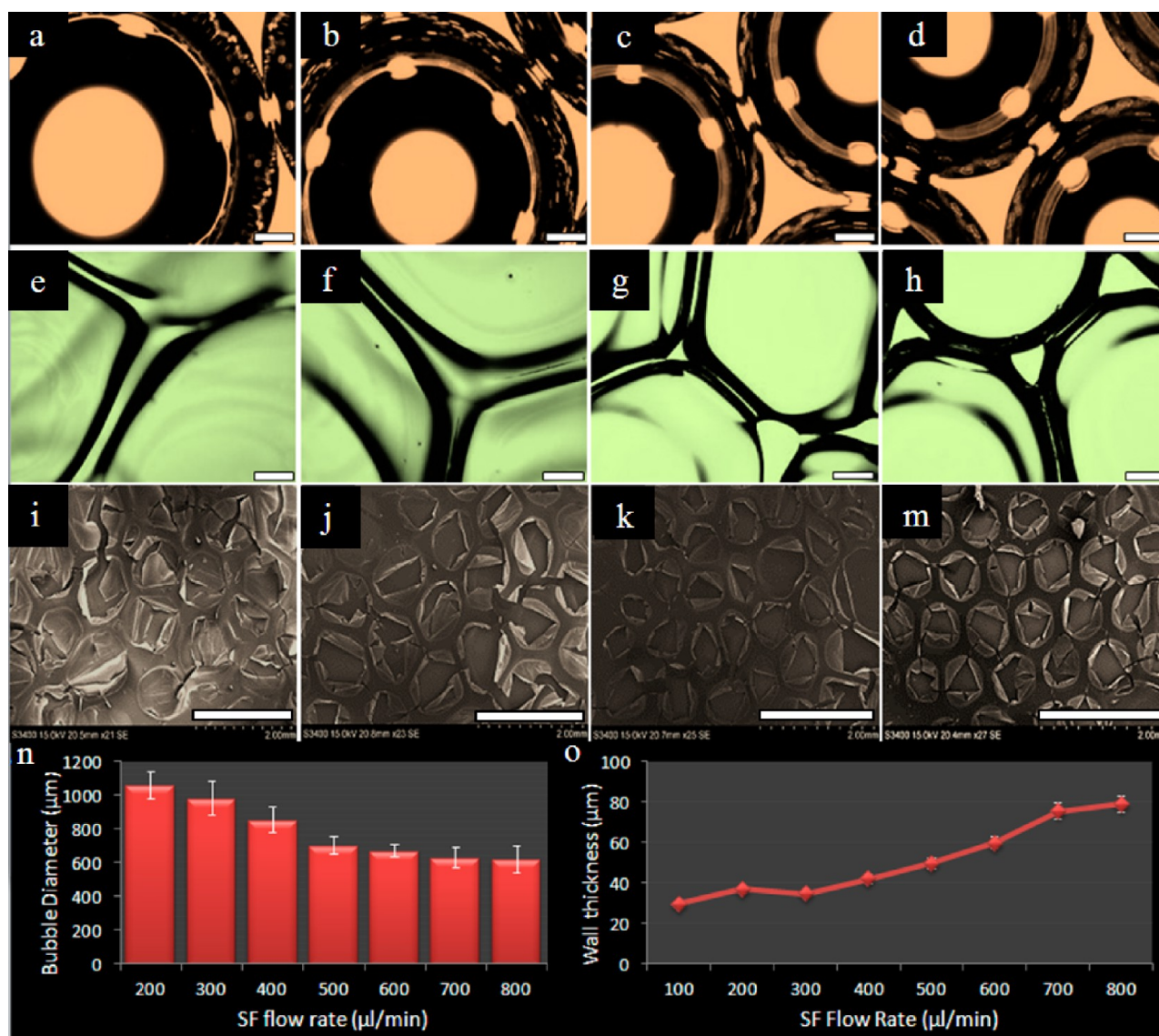


**Figure 5.** Effect of SF flow rates on bubble size at a constant air flow rate of  $2000 \mu\text{L min}^{-1}$ . (a–d) Optical images of bubble size with SF flow rate: (a) 200, (b) 300, (c) 500, and (d)  $600 \mu\text{L min}^{-1}$ ; (e–h) Corresponding optical micrographs of shell thicknesses; (i–m) Corresponding SEM images of monolayered bubbles; (n) Graph showing the relationship between SF flow rate and bubble size; (o) Graph showing the relationship between SF flow rate and shell wall thickness. Scale bars on optical images are  $100 \mu\text{m}$  and SEM images are  $2 \text{ mm}$ .

microbubbling. Microbubbling of SF/PEO 4:1 was initiated at a liquid flow rate of  $50 \mu\text{L min}^{-1}$  with an air flow rate of  $1000 \mu\text{L min}^{-1}$  at  $20 \text{ kV}$ . The bubbles produced with these parameters had a mean diameter of  $\sim 75 \mu\text{m}$ , however, with a polydispersity index (PI) of 29% (Figure 7a). As EHD-microbubbling offers a potential to optimize the microbubbling process further (by significantly reducing the PI), the liquid flow rate was increased to  $100 \mu\text{L min}^{-1}$  with a constant air flow rate and applied voltage. The resulting bubbles were bigger in size, with an average diameter of  $92 \mu\text{m}$  and a PI of 18% (Figure 7b). It was evident that a higher liquid flow rate increased the uniformity of the bubbles, although this also increased bubble size. When the air flow rate was increased to  $2000 \mu\text{L min}^{-1}$ , with a liquid flow rate of  $100 \mu\text{L min}^{-1}$  and a voltage of  $20 \text{ kV}$ , the SF/PEO bubbles had an average diameter of  $170 \mu\text{m}$ , nearly twice the diameter of those generated earlier at  $100 \mu\text{L min}^{-1}$ . When the air flow rate was  $1000 \mu\text{L min}^{-1}$ , near monodisperse bubble generation (PI 5%) was achieved

(Figure 7c,d). The crucial shift from high PI to low PI can easily be achieved by simple parametric adjustments.

**Microbubbling of SF/BSA.** Compared to the SF/PEO blend, even fewer jetting instabilities were encountered with the addition of BSA to SF (1:1 volume ratio), and the corresponding parametric plot is shown in Figure 8.

Previously, BSA has been subjected to EHD processing to produce templates for porous structures with controllable porosities between  $\sim 400$  to  $950 \mu\text{m}$  and low PI obtained using various concentrations of BSA.<sup>25</sup> Bubbling of 20 wt % BSA produced a mean pore diameter of  $470 \mu\text{m}$ . BSA bubbles exhibit a brittle nature once dried, unless a chemical cross-linker is used.

A liquid flow rate of  $50 \mu\text{L min}^{-1}$  was the starting point for microbubbling SF/BSA with an air flow rate of  $2000 \mu\text{L min}^{-1}$  at  $12 \text{ kV}$ . Bubbles produced using these parameters had a mean diameter of  $370 \mu\text{m}$  with a PI of 13% (Figure 9a). Although apparently uniform, bubbles were not dense enough in terms of population, which would not suffice for an ordered structure

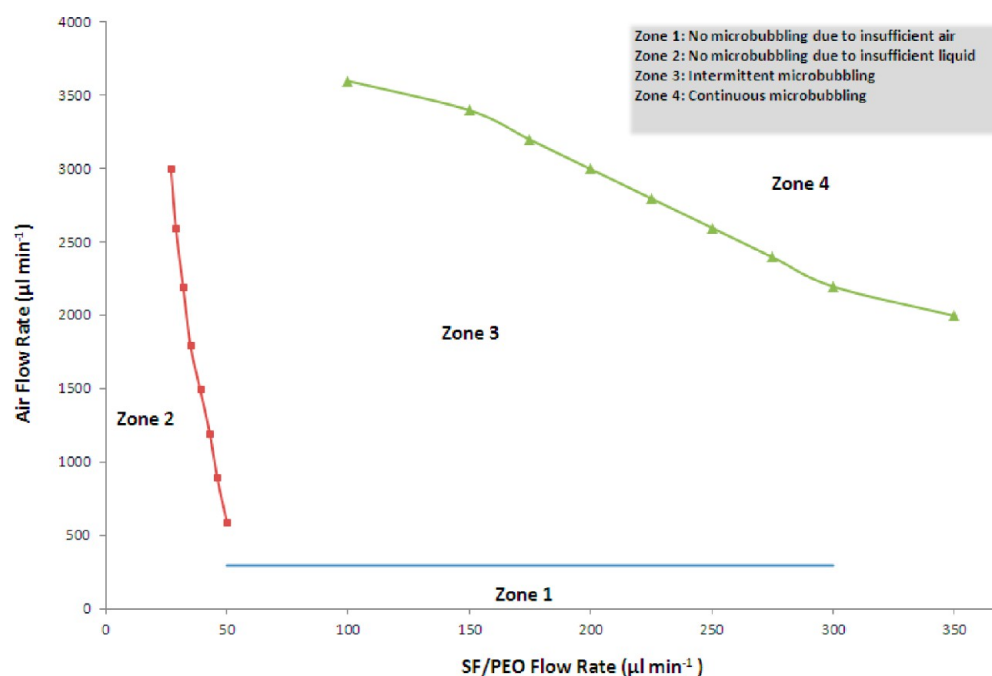


**Figure 6.** Parametric plot between the air flow rate and the flow rate of the SF/PEO blend.

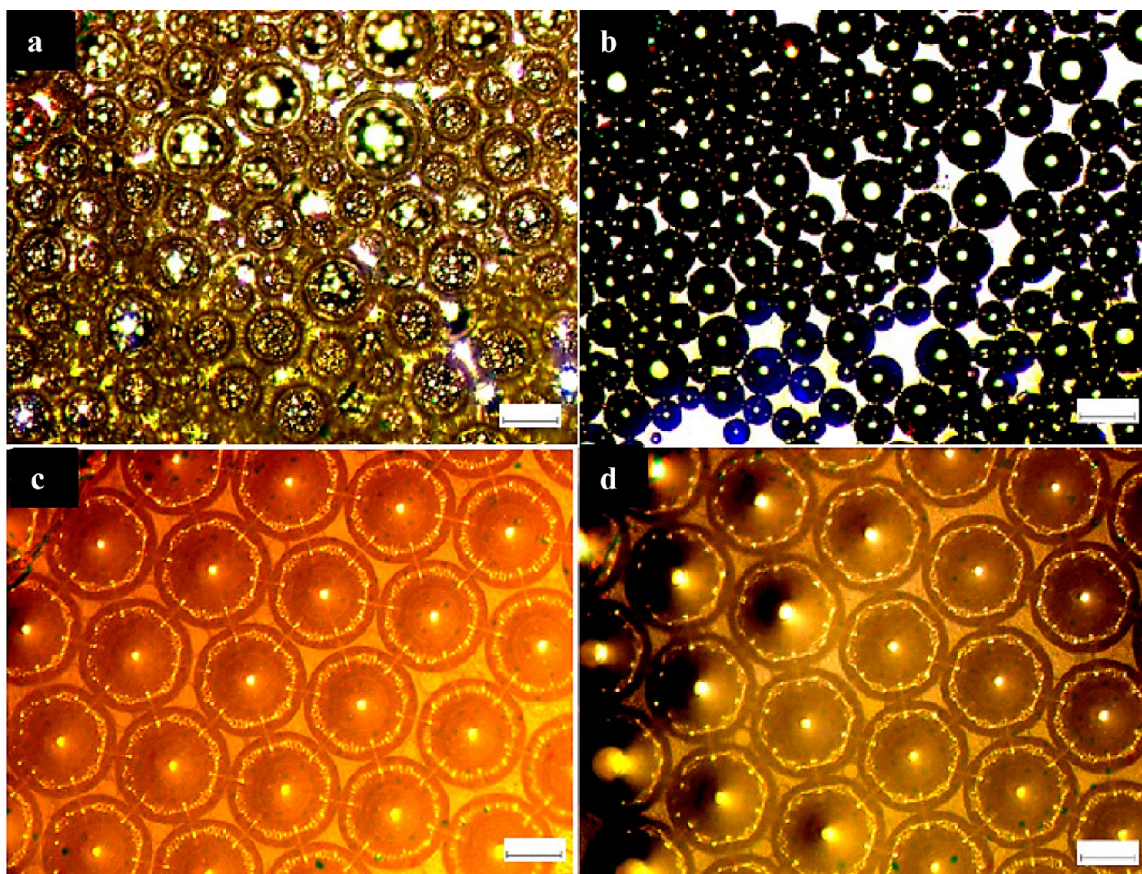


**Figure 7.** Optical images of the optimization process toward uniform microbubbles from a SF/PEO blend with (a) 50  $\mu\text{L min}^{-1}$  blend flow rate and air flow rate of 1000  $\mu\text{L min}^{-1}$ ; (b) 100  $\mu\text{L min}^{-1}$  blend flow rate and air flow rate of 1000  $\mu\text{L min}^{-1}$ ; and (c, d) 100  $\mu\text{L min}^{-1}$  blend flow rate and air flow rate of 2000  $\mu\text{L min}^{-1}$  taken from two different samples. All bubbles were generated at an applied electric field of 20 kV. Scale bars are 100  $\mu\text{m}$ .

when dried. When the liquid flow rate was lowered to 40  $\mu\text{L min}^{-1}$ , as expected, the bubble size decreased to  $\sim 200 \mu\text{m}$  with a PI of 20% (Figure 9b). Lowering the liquid flow rate further

to 20  $\mu\text{L min}^{-1}$  resulted in even smaller bubbles with a mean size of  $\sim 120 \mu\text{m}$  with a PI of 17% (Figure 9c). Finally, a liquid flow rate of 40  $\mu\text{L min}^{-1}$  and an air flow rate of 3000  $\mu\text{L min}^{-1}$



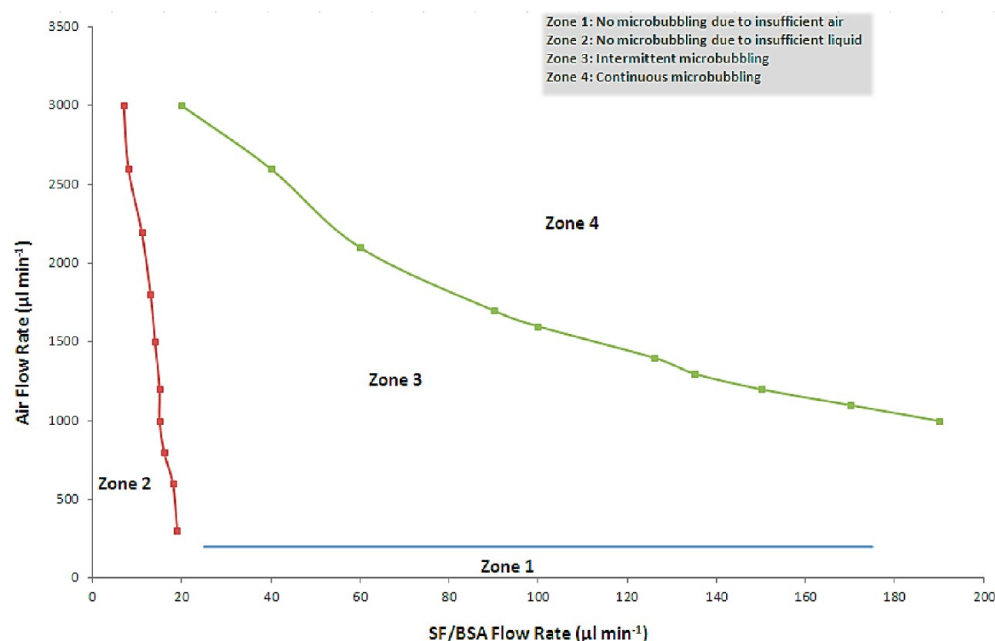


**Figure 8.** Parametric plot between the air flow rate and the flow rate of the SF/BSA blend.

at 11 kV generated highly uniform bubbles of 8% PI and mean diameter of 240  $\mu\text{m}$  (Figure 9d,e). SF/BSA bubbles displayed a different morphology when compared to SF and SF/PEO bubbles. The bubble shells and the struts in Figure 9f show spontaneous micropore formation. This could be due to the solvent phosphate buffered saline or a combination of these factors. Micropores within the structure can be beneficial in biomedical applications as they can be used to modify the degradation properties of the structure and enhance adherence to cells. The shape of the bubbles was initially spherical, changing to hexagonal upon collection (Figure 9g), which is very much related to the local surface tension of bubble coatings.<sup>37</sup>

**Analysis of SF Films.** Both cast and microbubbled SF films were analyzed using FT-IR to see if the processing method had any effect on the protein structure. Cast silk had an absorption band around 1637  $\text{cm}^{-1}$  (Figure 10a), films fabricated from microbubbling at SF flow rate 200  $\mu\text{L min}^{-1}$  and air flow rates of 2000 (Figure 10b), 4000 (Figure 10c), and 6000 (Figure 10d)  $\mu\text{L min}^{-1}$  had peaks at 1624  $\text{cm}^{-1}$  of the amide I region corresponding to  $\beta$ -sheet conformations. Strong peaks of 1521  $\text{cm}^{-1}$  were observed in all microbubbled films corresponding to  $\beta$ -sheet conformations in the amide II region followed by an absorption band at around 1230  $\text{cm}^{-1}$  corresponding to random coils at the amide III band shift.<sup>38</sup> It was notable that films which were formed with higher flow rates of air showed enhanced peaks of  $\beta$ -sheet conformation in both amide I and II regions.

This indicates that there were more  $\beta$ -sheet structures formed when microbubbling was performed at a higher air flow rate. The structure of the SF gives it the tendency to form  $\beta$ -sheets under certain conditions (e.g., utilizing methanol, acidic pH treatments), and applying higher shear rate induces the formation of intermolecular interactions.<sup>29</sup> Increased shear rates; whereby  $\beta$ -sheets are more ordered and orientated can be correlated with the bubbling process, that is, with increased air flow rates due to added shear; this also influences the  $\beta$ -sheet packing of SF. This increase in  $\beta$ -sheets with increase in air flow

rate can be explained by the increased shear-gradient due to high air flow rates and, hence, turbidity, leading to  $\beta$ -sheet rich silk macromolecule clusters to be dispersed facilitating intermolecular self-assembly.<sup>34</sup> Natural fiber formation is a result of shearing and extensional flow in silk worms. This extensional flow could be mimicked by the microbubbling process causing alignments of the  $\beta$ -sheets in an aqueous environment. Another possible mechanism to explain this could be that the proteins bond to one another side-by-side through cross-links that could add to the stability. This process could serve as an alternative route to enhance mechanical properties of SF and, most importantly, during processing.

Following FT-IR analysis, the films were tested for their tensile properties. In this study, incorporation of porosity to the SF films (via microbubbling) resulted in a tensile strength of  $3.4 \pm 0.1$  MPa obtained with an air flow rate of 2000  $\mu\text{L min}^{-1}$  at an average film thickness of 30  $\mu\text{m}$ . The mean pore size at this flow rate was 740  $\mu\text{m}$ , with a mean strut thickness of 230  $\mu\text{m}$ . When the air flow rate was increased to 4000  $\mu\text{L min}^{-1}$ , the tensile strength of the films obtained decreased substantially by 71% to  $0.63 \pm 0.3$  MPa, with a doubled mean pore size of 1500  $\mu\text{m}$  and a mean strut thickness of 170  $\mu\text{m}$ . Further increase in the air flow rate to 6000  $\mu\text{L min}^{-1}$  resulted in a tensile strength of  $0.03 \pm 0.05$  MPa, with a decrease in strength of 99% compared to the initial flow rate and with a mean pore size of 1800  $\mu\text{m}$  and a mean strut thickness of 60  $\mu\text{m}$ .

Although the  $\beta$ -sheet packing is enhanced during the EHD-microbubbling process with increased air flow rates, the larger pore formation reduces the tensile strength of the overall structure. As the air flow rate is increased, the struts around pores (bubbles) become progressively thinner, leading to a more flexible film compared to a lower air flow rate where the pore size is smaller, making larger struts (Figure 11). Parametric changes during the bubble forming process can therefore regulate intermolecular  $\beta$ -sheet packing and also the overall porosity of the structure, which in turn determines the mechanical properties. In addition to this, the density of materials is also reduced when the pore size (air flow rate) is



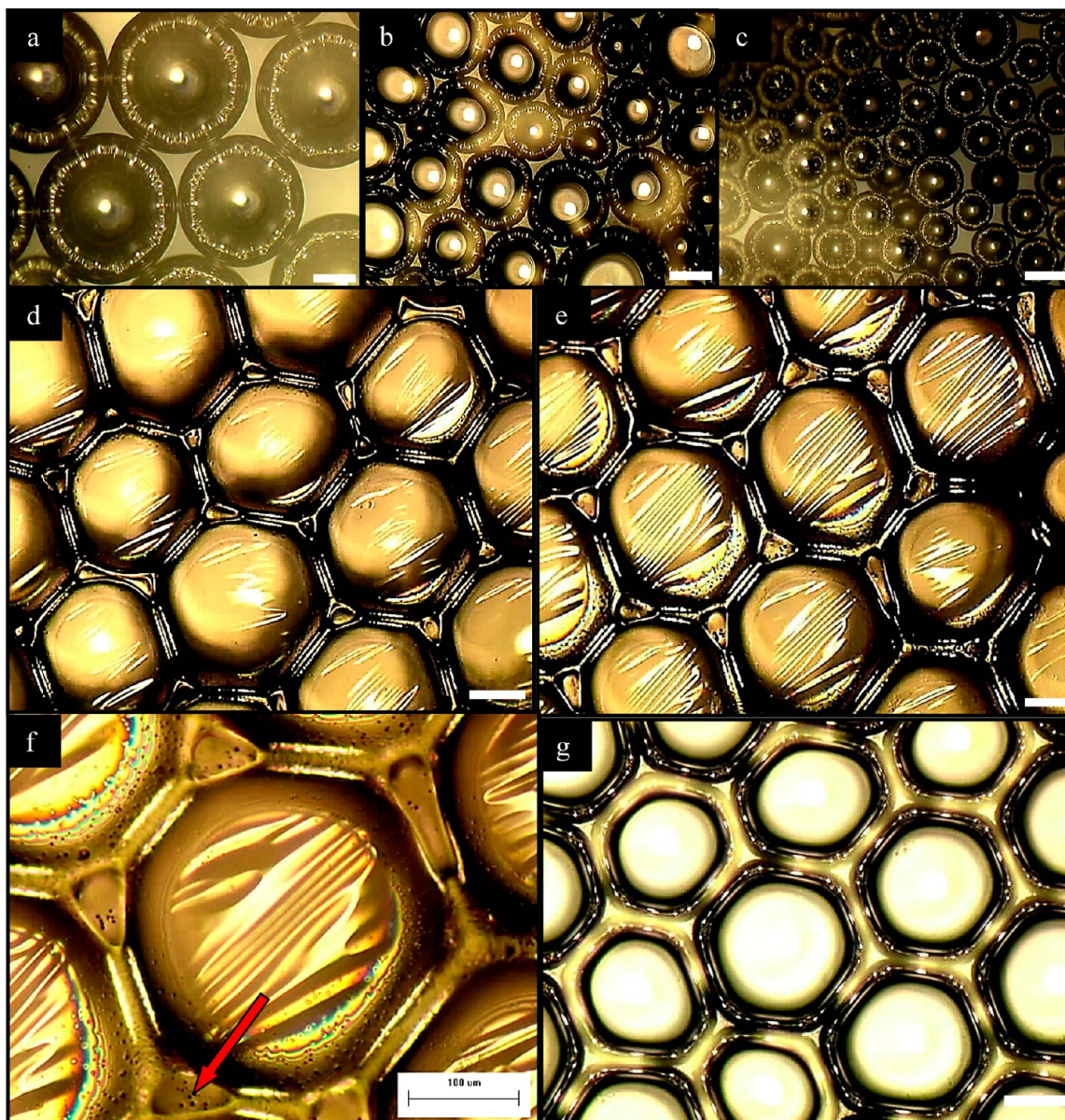


**Figure 9.** Optical images of the optimization process toward uniform microbubbles from the SF/BSA blend at 11–12 kV: (a)  $50 \mu\text{L min}^{-1}$  blend flow rate and air flow rate of  $2000 \mu\text{L min}^{-1}$ ; (b)  $40 \mu\text{L min}^{-1}$  blend flow rate and air flow rate of  $2000 \mu\text{L min}^{-1}$ ; (c)  $20 \mu\text{L min}^{-1}$  blend flow rate and air flow rate of  $2000 \mu\text{L min}^{-1}$ ; (d, e)  $40 \mu\text{L min}^{-1}$  blend flow rate and air flow rate of  $3000 \mu\text{L min}^{-1}$ ; (f) higher magnification ( $\times 10$ ) of the bubble; and (g) bubble view under reflected light. Scale bars are  $100 \mu\text{m}$ . Red arrow points to the micropores.

increased, as there is less material per given volume of occupied structure.

## CONCLUSIONS

This work demonstrated that SF and various SF blends are suitable for microbubbling with various sizes ( $75\text{--}1000 \mu\text{m}$ ) and size distributions of bubbles being formed. The processing parameters and properties of the solutions play an important role in optimizing structures. In the present study, the results of EHD-microbubbling aqueous SF, SF/PEO, and SF/BSA blends were mapped. Following optimization of the EHD-microbubbling process to eliminate gelling and fiber formation, precise control over the final structures was obtained. A uniform bubble size of  $\sim 600 \mu\text{m}$  was achieved with aqueous SF. Microbubbling of the SF/PEO blend resulted in a bubble size of  $170 \mu\text{m}$  with 5% polydispersity.

Microbubbling of SF/BSA resulted in a unique morphology compared to the aqueous SF and SF/PEO blends. A bubble size of  $240 \mu\text{m}$  with 8% polydispersity was obtained. Micropore formation was observed in the structures obtained probably due to the phosphate buffered saline used in the BSA solution. The successful bubbling process of BSA has shown that other bioactive proteins such as drugs can be blended with SF and microbubbled to fabricate porous structures with drug delivery capabilities.

An interesting finding from the FT-IR spectra of the microbubbled pure silk films compared to the cast film was that microbubbling at higher air flow rates enhanced  $\beta$ -sheet formation. This could be attributed to the fact that the shear forces subjected by microbubbling are aligning the  $\beta$ -sheets further which is known to enhance the mechanical properties of the bulk structure. The findings presented here can also be used

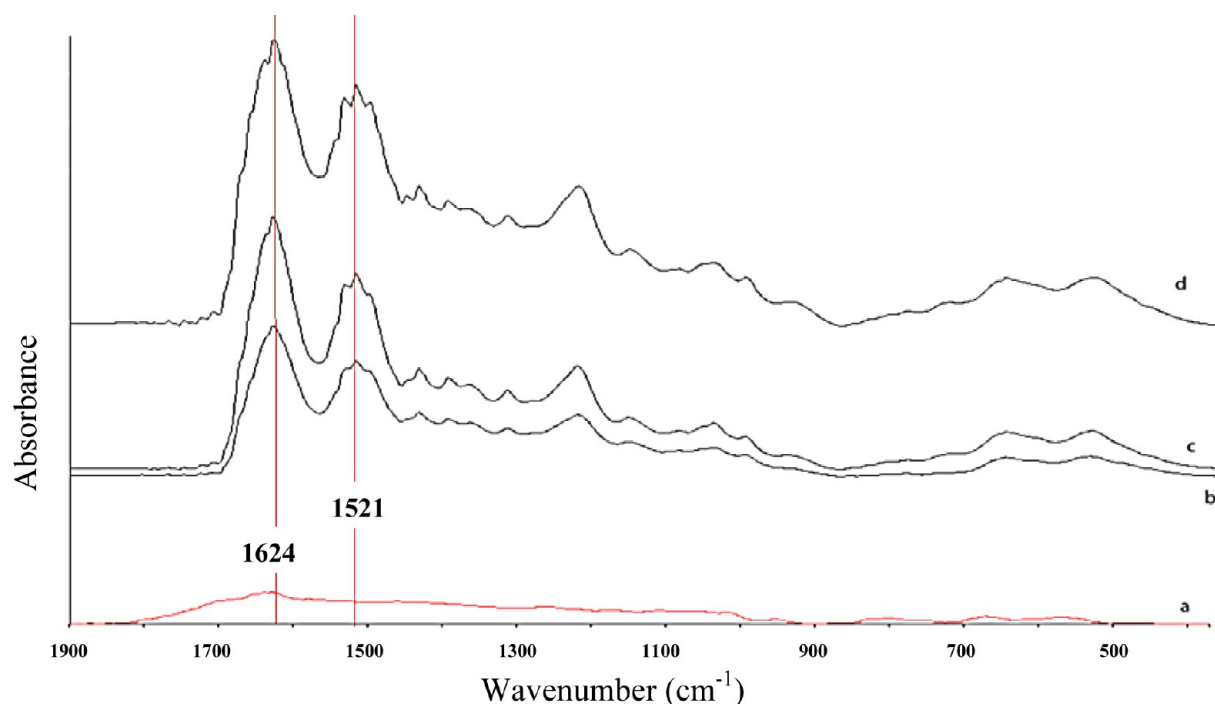


**Figure 10.** FT-IR spectra of SF films obtained by (a) casting and microbubbling processes under different air flow rates of (b) 2000, (c) 4000, and (d) 6000  $\mu\text{L min}^{-1}$ .

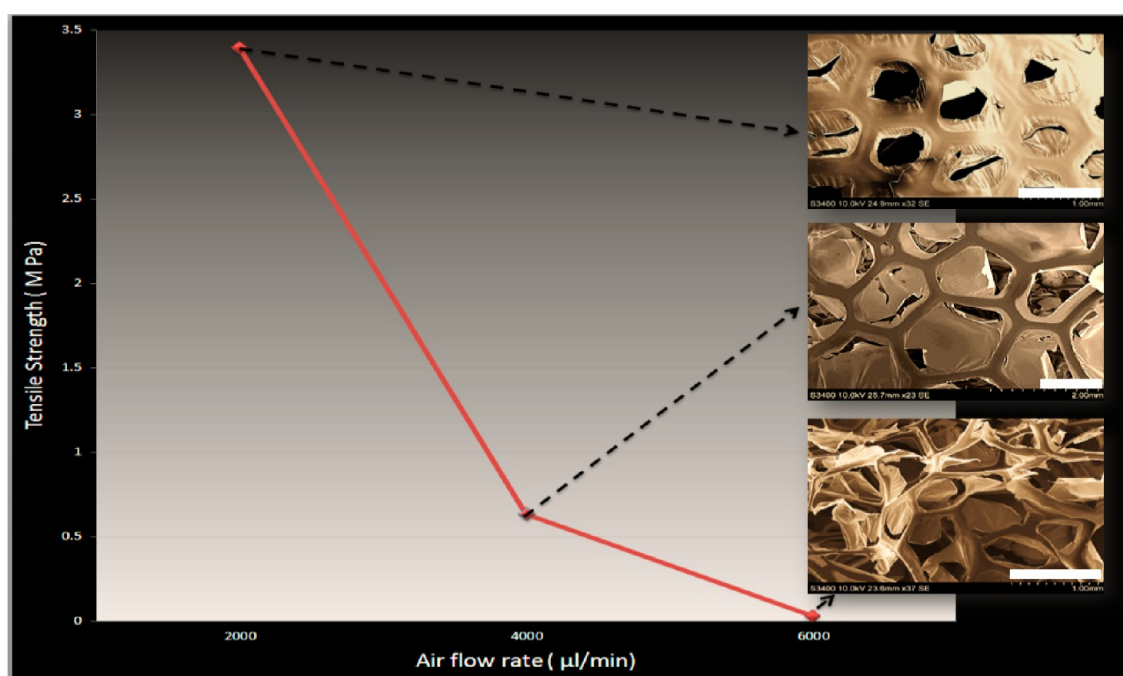


**Figure 11.** Tensile properties of pure SF films produced with air flow rates of 2000, 4000, and 6000  $\mu\text{L min}^{-1}$ . Scale bars are 1 mm.

as an alternative method of aligning  $\beta$ -sheets during processing, without the need of an additional step. However, mechanical testing concludes that porous films formed using a lower air flow rate had higher tensile strength as the porosity plays the key role in determining strength.

SF is an ideal material for biomedical applications, either used alone or as a reinforcing composite agent with other biomaterials for specific applications. The EHD-microbubbling process is capable of generating bubbles to produce controlled porous structures by the transformation of what initially were

bubbles to self-templates. The SF-based solutions can easily be infused through the outer needle of the device to form the shell of the bubbles where size and uniformity can be controlled. With the invention of the processing method described in this paper, future work is focused toward the biomedical applicability of the structures and the incorporation of functionalizing or active agents (hydroxyapatite, drugs or cells) in the SF blends for making of bone tissue engineering scaffolds utilizing the EHD-microbubbling process.



## AUTHOR INFORMATION

### Corresponding Author

\*E-mail: david.kaplan@tufts.edu; m.edirisinghe@ucl.ac.uk.

### Notes

The authors declare no competing financial interest.

## ACKNOWLEDGMENTS

We would like to thank the University College London (UCL) Archaeology Department for the use of their electron microscopes and FT-IR. We would also like to thank, CJ Luo and Cem Bayram for their helpful discussions and Bilal Saeed Ahmad for his help with rheology measurement. Z.E. would like to thank UCL for partially funding her doctoral research work.

## REFERENCES

- (1) Langer, R.; Vacanti, J. P. *Science* **1993**, *260*, 920–926.
- (2) Bettinger, C. J.; Cyr, K. M.; Matsumoto, A.; Langer, R.; Borenstein, J. T.; Kaplan, D. L. *Adv. Mater.* **2007**, *19*, 2847–2850.
- (3) Omenetto, F. G.; Kaplan, D. L. *Science* **2010**, *329*, 528–531.
- (4) Cao, Y.; Wang, B. *Int. J. Mol. Sci.* **2009**, *10*, 1514–1524.
- (5) Zhao, S.; Zhou, Z.; Wu, J.; Wang, S.; Guo, X.; Zhang, Q. *J. Compos. Mater.* **2012**, *46*, 1571–1581.
- (6) Chen, J.-P.; Chen, S.-H.; Lai, G.-J. *Nanoscale Res. Lett.* **2012**, *7*, 1–11.
- (7) Yang, Z.; Xu, L. S.; Yin, F.; Shi, Y. Q.; Han, Y.; Zhang, L.; Jin, H. F.; Nie, Y. Z.; Wang, J. B.; Hao, X.; Fan, D. M.; Zhou, X. M. *J. Dig. Dis.* **2012**, *13*, 168–178.
- (8) Hu, J.; Chen, B.; Guo, F.; Du, J.; Gu, P.; Lin, X.; Yang, W.; Zhang, H.; Lu, M.; Huang, Y.; Xu, G. *Mater. Sci.: Mater. Med.* **2012**, *23*, 711–722.
- (9) Pritchard, E. M.; Kaplan, D. L. *Expert Opin. Drug Delivery* **2011**, *8*, 797–811.
- (10) Rockwood, D. N.; Preda, R. C.; Yucel, T.; Wang, X.; Lovett, M. L.; Kaplan, D. L. *Nat. Protoc.* **2011**, *6*, 1612–1631.
- (11) Wang, M.; Jin, H. J.; Kaplan, D. L.; Rutledge, G. C. *Macromolecules* **2004**, *37*, 6856–6864.
- (12) Cao, H.; Chen, X.; Huang, L.; Shao, Z. *Mater. Sci. Eng., C* **2009**, *29*, 2270–2274.
- (13) Fan, L.-p.; Zhang, K.-h.; Sheng, X.-y.; Wu, C.-c.; Li, J.; Mo, X.-m.; Wang, H.-s., 2010 International Forum on Biomedical Textile Materials; Donghua Univ., Songjian Campus, Shanghai, May 28–29, 2010. In *Electrospinning and Post-Spin Treatment of Regenerated Silk Fibroin Nanofibers*, 2010, 96–100.
- (14) Huang, J.; Liu, L.; Yao, J. *Fibers Polym.* **2011**, *12*, 1002–1006.
- (15) Wu, Y.; MacKay, J. A.; McDaniel, J. R.; Chilkoti, A.; Clark, R. L. *Biomacromolecules* **2009**, *10*, 19–24.
- (16) Enayati, M.; Chang, M. W.; Bragman, F.; Edirisinghe, M.; Stride, E. *Colloids Surf., A* **2011**, *382*, 154–164.
- (17) Chakraborty, S.; Liao, I. C.; Adler, A.; Leong, K. W. *Adv. Drug Delivery Rev.* **2009**, *61*, 1043–1054.
- (18) Ahmad, Z.; Thian, E. S.; Huang, J.; Edirisinghe, M. J.; Jayasinghe, S. N.; Best, S. M.; Bonfield, W.; Brooks, R. A.; Rushton, N. *J. Mater. Sci.: Mater. Med.* **2008**, *19*, 3093–3104.
- (19) Enayati, M.; Ahmad, Z.; Stride, E.; Edirisinghe, M. J. *R. Soc. Interface* **2010**, *7*, 667–675.
- (20) Farook, U.; Zhang, H. B.; Edirisinghe, M. J.; Stride, E.; Saffari, N. *Med. Eng. Phys.* **2007**, *29*, 749–754.
- (21) Li, L.; Wei, Q.; Li, H.-B.; Wen, S.; Teng, G.-J. *Plos One* **2012**, *7*, 1–6.
- (22) Zheng, H. J. *Acoust. Soc. Am.* **2012**, *131*, 3245.
- (23) Nair, A.; Thevenot, P.; Dey, J.; Shen, J. H.; Sun, M. W.; Yang, J.; Tang, L. P. *Tissue Eng., Part C* **2010**, *16*, 23–32.
- (24) Ekemen, Z.; Ahmad, Z.; Edirisinghe, M.; Stride, E. *Macromol. Mater. Eng.* **2011**, *296*, 8–13.
- (25) Ekemen, Z.; Chang, H.; Ahmad, Z.; Bayram, C.; Rong, Z.; Denkbass, E. B.; Stride, E.; Vadgama, P.; Edirisinghe, M. *Biomacromolecules* **2011**, *12*, 4291–4300.
- (26) Kim, U. J.; Park, J.; Kim, H. J.; Wada, M.; Kaplan, D. L. *Biomaterials* **2005**, *26*, 2775–2785.
- (27) Nazarov, R.; Jin, H. J.; Kaplan, D. L. *Biomacromolecules* **2004**, *5*, 5718–5726.
- (28) Jin, H. J.; Chen, J.; Karageorgiou, V.; Altman, G. H.; Kaplan, D. L. *Biomaterials* **2004**, *25*, 1039–1047.
- (29) Johnston, J. H. *Biochem. J.* **1927**, *21*, 1314–1328.
- (30) Jin, H. J.; Kaplan, D. L. *Nature* **2003**, *424*, 1057–1061.
- (31) Wang, Q.; Yang, Y.; Chen, X.; Shao, Z. *Biomacromolecules* **2012**, *13*, 1875–1881.
- (32) Zhou, C. Z.; Confalonieri, F.; Medina, N.; Zivanovic, Y.; Esnault, C.; Yang, T.; Jacquet, M.; Janin, J.; Duguet, M.; Perasso, R.; Li, Z. G. *Nucleic Acids Res.* **2000**, *28*, 2413–2419.
- (33) Wang, X.; Kluge, J. A.; Leisk, G. G.; Kaplan, D. L. *Biomaterials* **2008**, *29*, 1054–1064.
- (34) Yucel, T.; Cebe, P.; Kaplan, D. L. *Biophys. J.* **2009**, *97*, 2044–2050.
- (35) Farook, U.; Stride, E.; Edirisinghe, M. J.; Moaleji, R. *Med. Biol. Eng. Comput.* **2007**, *45*, 781–789.
- (36) Farook, U.; Stride, E.; Edirisinghe, M. J. *J. R. Soc. Interface* **2009**, *6*, 271–277.
- (37) Yang, Y.; Dicko, C.; Bain, C. D.; Gong, Z.; Jacobs, R. M. J.; Shao, Z.; Terry, A. E.; Vollrath, F. *Soft Matter* **2012**, *37*, 9705–9712.
- (38) Lu, Q.; Hu, X.; Wang, X.; Kluge, J. A.; Lu, S.; Cebe, P.; Kaplan, D. L. *Acta Biomater.* **2010**, *6*, 1380–1387.